

Thin film notch filters as platforms for biological image processing

Shaban B. Sulejman,^{1, a)} Niken Priscilla,^{1, b)} Lukas Wesemann,¹ Wendy S. L. Lee,^{1, 2}
Jieqiong Lou,³ Elizabeth Hinde,³ Timothy J. Davis,¹ and Ann Roberts¹

¹⁾*ARC Centre of Excellence for Transformative Meta-Optical Systems,
School of Physics, The University of Melbourne, Victoria 3010,
Australia.*

²⁾*ARC Centre of Excellence for Transformative Meta-Optical Systems,
Department of Electrical and Electronic Engineering, The University of Melbourne,
Victoria 3010, Australia.*

³⁾*School of Physics, The University of Melbourne, Victoria 3010,
Australia.*

Many image processing operations involve the modification of the spatial frequency content of images. Here we demonstrate object-plane spatial frequency filtering utilizing the angular sensitivity of a commercial spectral bandstop filter. This approach to all-optical image processing is shown to generate real-time pseudo-3D images of transparent biological and other samples, such as human cervical cancer cells. This work demonstrates the potential of non-local, non-interferometric approaches to image processing for uses in label-free biological cell imaging and dynamical monitoring.

^{a)}Electronic mail: sulejmans@unimelb.edu.au

^{b)}Electronic mail: niken.priscilla@unimelb.edu.au

I. INTRODUCTION

Transparent objects, including most biological cells, interact weakly with light resulting in little contrast in conventional bright field microscopy. However, spatial variations in their morphology and optical properties introduce local spatial phase variations onto light transmitted through them. In the simplest case, this can be characterized by a transmission function $O(x, y) \approx O_0 e^{i\varphi(x, y)}$. While the amplitude O_0 is approximately spatially invariant, the shape and refractive index information is contained in the phase function $\varphi(x, y)$. Such phase variations cannot be directly sensed by conventional cameras and requires indirect detection. Popular optical phase visualization methods include Zernike¹ and differential interference contrast microscopy². However, these can require expensive components or Fourier plane access that increases system complexity and size. Digital methods include ptychography^{3–5}, the use of the transport of intensity equation^{6–8} or phase retrieval algorithms such as the Gerchberg-Saxton⁹ and Fienup algorithms¹⁰. However, these are limited by their extensive computational requirements.

All-optical, object-plane image processing offers a non-interferometric compact alternative for phase visualization. It is enabled by 2D space-invariant linear optical systems, such as thin films^{11,12}, with angular responsivities that directly filter the spatial frequency of wavefields¹³. Unlike common computational or all-optical methods utilizing the classical $4f$ -configuration¹⁴, it avoids optical phase information losses, energy consuming post processing and bulky configurations associated with accessing Fourier planes. The importance of compact optical systems for all-optical, object-plane image processing is motivated by the potential for integration into portable devices. This can have applications as diverse as mobile diagnostics, environmental monitoring and remote sensing.

To explain how a device exhibiting angular dispersion can perform image processing, we ignore any polarization effects for simplicity. In this case, the impact of object-plane Fourier filtering on the spatial frequency spectrum of the field can be described by an optical transfer function $\mathcal{H}(k_x, k_y)$ ¹⁵. By taking the z -axis as the optical axis, k_x and k_y denote the transverse spatial frequency components of the wave-vector $\vec{k} = (k_x, k_y, k_z)$ and $k_z = \sqrt{|\vec{k}|^2 - k_x^2 - k_y^2}$. The transfer function relates the processed output to the input by the convolution theorem,

$$E_{\text{out}}(x, y, z) = \mathcal{F}^{-1} \{ \mathcal{H}(k_x, k_y) \tilde{E}_{\text{in}}(k_x, k_y; z) \} (x, y), \quad (1)$$

where \mathcal{F} denotes the Fourier transform, E represents any component of the electric field and $\tilde{E}_{\text{in}} \equiv \mathcal{F} \{ E_{\text{in}} \}$. For example, high-pass filters block low spatial frequencies to eliminate unscattered

field components for edge detection¹⁶, which is fundamental to data compression¹⁷ and machine vision^{18,19}. A notable sub-class is that of linear optical transfer functions, i.e. $\mathcal{H} \propto k_x$ or $\mathcal{H} \propto k_y$. These can directly translate phase gradients into intensity variations through spatial differentiation in the case of transparent objects to permit phase visualization¹¹. The influence of polarization can be incorporated into this approach by utilizing a 2×2 transfer function dyadic tensor.

The angular sensitivity provides the mechanism for image processing through the correspondence between angles of incidence and spatial frequencies. This is given by representing the spatial frequency components in spherical coordinates¹³,

$$\begin{aligned} k_x &= k_0 \sin \theta \cos \phi \\ k_y &= k_0 \sin \theta \sin \phi \\ k_z &= k_0 \cos \theta, \end{aligned} \tag{2}$$

where $k_0 = |\vec{k}|$ is the wavenumber, while (θ, ϕ) are the polar and azimuthal propagation angles of plane waves with respect to the z -axis. Given that optical transfer functions represent plane wave responses in k -space, and that light can be decomposed into weighted plane waves by the spatial Fourier transform^{13,20}, then devices exhibiting angular dispersive transmission are capable of object-plane image processing.

Recently, meta-optical devices have attracted considerable attention as ultra-compact image processors²¹. For example, Zhou et al.²² employed photonic crystals for edge detection of organic samples, while Wesemann et al.²³ obtained phase contrast images of human cancer cells using a resonant waveguide grating. Other approaches have involved Mie^{24,25} or Fano²⁶ resonances, photonic spin-orbit coupling effects^{27,28} and bound states in the continuum²⁹. With this rapidly growing interest in meta-optics, it is timely to consider other optical elements capable of performing an equivalent role. Earlier works have investigated various structures for edge detection such as volume hologram filters³⁰, Fabry-Pérot etalons³¹, detuned interference filters^{32–34}, acousto-optic modulators³⁵ and gratings^{36–38}. With the exception of Fourier plane phase contrast methods, the emergence of successful digital methods for image processing held back further progress in all-optical techniques.

Here we demonstrate the use of a commercially available thin film spectral notch filter applied to phase contrast imaging of weakly absorbing phase objects. Notch filters are band-stop filters commonly employed in various types of spectroscopy to remove temporal frequencies over a specific range^{39,40}. We show that the angular dispersion of the filter's rejection band produces a high-

pass spatial frequency filter at the operating wavelength. Introducing a phase bias by tilting the filter with respect to the optical axis can produce pseudo-three dimensional images similar to those obtained in differential interference contrast microscopy. Moreover, the contrast generated is determined by the rotation axis and angle. We demonstrate enhanced contrast imaging of wavefields introduced by a spatial light modulator and unstained biological samples, including human cervical cancer cells. Our results confirm real-time phase contrast imaging without post-processing, permitting direct imaging with either a camera or the eye. This method provides a novel all-optical approach for biological and other image processing using off-the-shelf band-stop devices. It has the potential for developments in machine vision, biological imaging and dynamical monitoring.

II. EXPERIMENTAL METHODS & RESULTS

A. Device Performance

The device investigated here is a commercially obtained notch filter (Thorlabs NF633-25), which has a specified central operating wavelength of 633 nm and band-width of 25 nm at normal incidence. Transmission spectra as a function of angle of incidence were experimentally measured using the configuration in Fig. 1, with details provided in the supplementary information (§S2A). The results (Fig. 2(a)) obtained using circularly polarized light are consistent with the manufacturer's specifications. Meanwhile, the results for p - and s -polarized light are given in the supplementary material (§2A). Noting the correspondence between (θ, ϕ) and (k_x, k_y) , it is found that the notch filter suppresses low spatial frequencies associated with near-normal incidence angles at the band-stop wavelength.

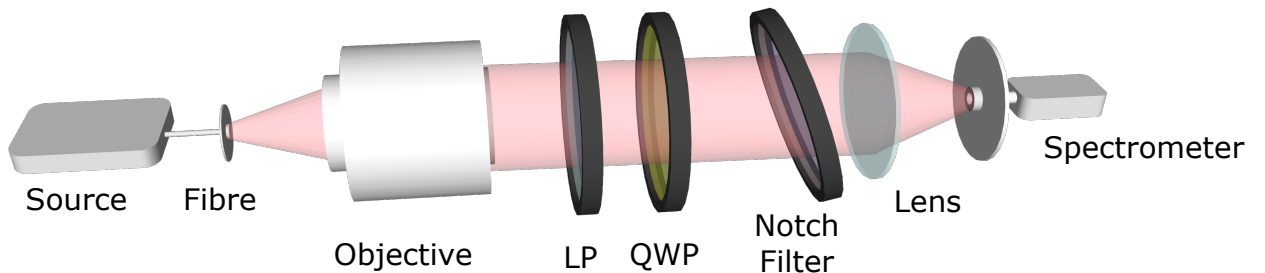


FIG. 1. The experimental configuration used to capture transmission spectra of the notch filter. Here, LP and QWP denote linear polarizer and quarter wave-plate, respectively.

Modulation transfer functions $|\mathcal{H}(k_x, k_y)|$ were mapped from the measured transmission spec-

tra for p -, s - and circular polarizations. Line profiles along $k_y = 0$ (Fig. 2(b)) at the band-stop wavelength exhibit approximately polarization-insensitive, high-pass behaviour with a suppression zone of numerical aperture (NA) range ~ 0.2 . This is produced by the blue-shifting of the band-stop wavelength with increasing angle of incidence.

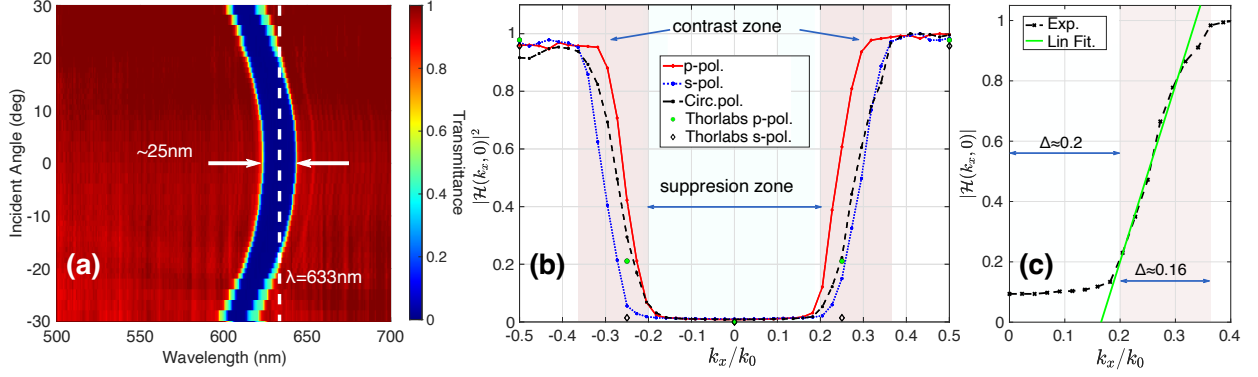


FIG. 2. The experimental transmission spectra obtained by incrementally rotating the filter is given in (a). The modulation transfer function along $k_y = 0$ produces the plot shown in (b) for various polarizations, which is compared to data provided by the manufacturer. Linear fitting of the modulation transfer function in the contrast zone is given in (c).

A significant feature of the device is the region of approximate linear dependence on k_x from zero to near-unity transmission beyond the suppression zone. This is supported by linear fitting (Fig. 2(c)) from $k_x/k_0 \sim 0.2$ to 0.3 , represented by the relation $Ak_x/k_0 + B$. The polyfit function and curve fitting toolbox in MATLAB were used to obtain the fitting parameters and their error intervals as $A = 5.9 \pm 0.83$ and $B = -0.97 \pm 0.22$. Rotating the filter by 12° about a line perpendicular to the optical axis shifts operation to $k_x/k_0 \approx \pm 0.2$ to access this region, referred to here as the contrast zone. Such a linear optical transfer function substituted into Eq. (1) approximately produces the spatial derivative around an intensity offset along the axis of rotation. This can generate intensity images directly related to phase gradients¹³, given by

$$\nabla O(x, y) \approx iO_0(\nabla\phi(x, y))e^{i\phi(x, y)}. \quad (3)$$

Consequently, intensity contrast is created in regions where the phase is varying along the relevant direction by the direct relationship in Eq. (3). Operating near the edge of the contrast zone removes unscattered field components leaving only relatively large phase gradients that enhance edges. However, operating within the contrast zone at a rotation angle of 14° , corresponding to

$k_x/k_0 \approx 0.24$, preserves some unscattered components and enables discrimination between positive and negative phase gradients. These manifest as different grayscale levels above or below the shifted k -space origin, respectively. Therefore, operation within the contrast zone enables phase visualization by converting phase gradients to intensity. This includes information about the sign of the gradient to produce pseudo-3D images. Phase gradients along different directions can also be visualized by changing the axis of rotation. These form the key underpinnings of this paper to describe the capacity of notch filters for phase visualization.

B. Phase Contrast Imaging

All-optical image processing was experimentally performed on various samples with the notch filter using circularly polarized, 635 nm laser light. Edge detection of amplitude objects was first demonstrated on a USAF resolution test target, with details and results provided in the supplementary information (§S2B). Phase imaging was then performed using the configuration (Fig. 3) detailed in the supplementary information (§S2C). A computer-controlled spatial light modulator emulated phase profiles of human red blood cells (Fig. 4(a)), which were modelled using the properties obtained from Ref. 41. Collimated light reflected from the spatial light modulator passed through the notch filter, which was rotated within the focal plane between paired microscope objectives. A camera then captured the transmitted images.

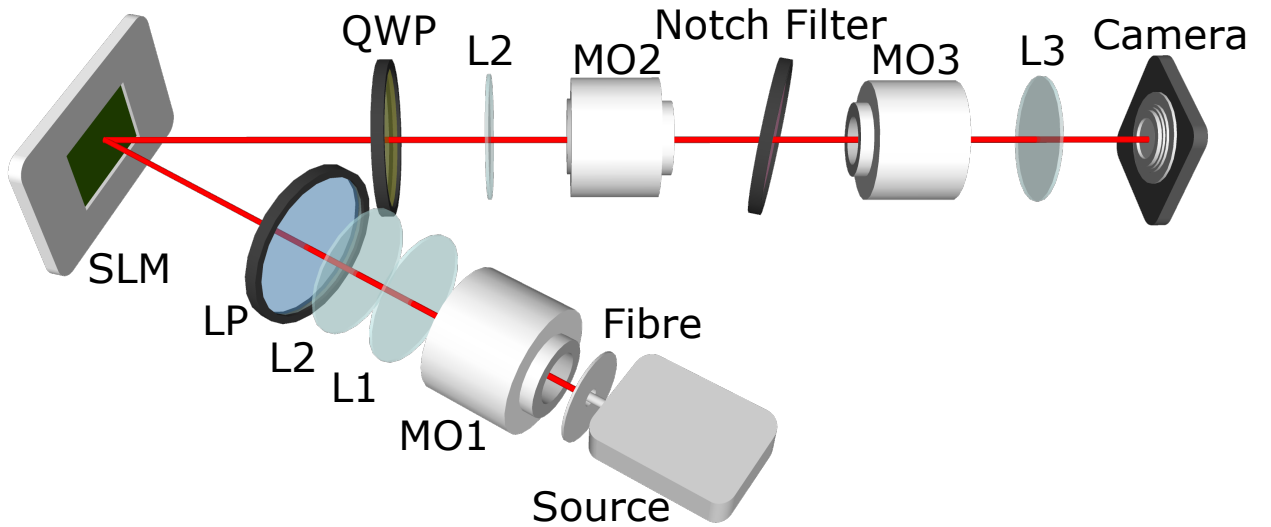


FIG. 3. The configuration for image processing with a spatial light modulator (SLM), where L and MO denote lenses and microscope objectives, respectively.

The results are presented in Fig. 4(b)-(e), where simulated and experimental images are compared. An experimental control image without the filter (Fig. 4(b)) displays poor contrast, rendering the object virtually invisible as expected for weakly absorbing phase objects. Simulated and experimental phase images (Fig. 4(c) and (d)) are obtained by introducing the filter at a rotation angle of 14° . These preserved some unscattered contributions leading to the appearance of pseudo-3D phase contrast. Moreover, the simulated phase image (Fig. 4(c)) is consistent with experiment (Fig. 4(d)). In both cases, regions where a change in phase is present, i.e. $\nabla\phi(x,y) \neq 0$, are transformed to intensity variations arising from otherwise invisible phase modulations. Moreover, ringing artifacts associated with the Gibbs phenomenon can also be seen. The resultant images additionally possess the capacity to distinguish between positive and negative phase gradients. Furthermore, line profiles (Fig. 4(e)) exhibit intensity variations associated with phase variation introduced into the field by the sample. Some intensity artifacts can also be seen, such as those arising from amplitude variations in the field.

To illustrate potential microscopy applications, phase contrast microscopy images were obtained of biological samples with weak amplitude contrast. This was performed using an inverted microscope configuration depicted in Fig. 5(a). Moreover, human cervical cancer (HeLa) cells were used as the sample and the preparation steps are outlined in the supplementary information (§S2E). Their bright field image (Fig. 5(b)) displays little to no contrast. However, placing the notch filter immediately beneath the sample enabled visualization of the phase variations when illuminated with 635 nm laser light. The phase contrast image (Fig. 5(c)) obtained within the contrast zone contains morphological detail absent in the corresponding bright field image, such as those highlighted within the green curves. The contrast produced exhibits significantly enhanced phase visualization compared to the relatively low contrast bright field image. Cellular thickness and local refractive index deviations are accentuated to discriminate the cells from their background. A conventional differential interference contrast image was also taken of the same regions, which is given in the supplementary information (§S2D) as a baseline for comparison.

III. DISCUSSION

Inspired by the recent surge in interest towards meta-optical imaging, these results represent the first demonstration of biological image processing using a commercially available filter. The spatial frequency content of images was directly altered by the notch filter in the object plane

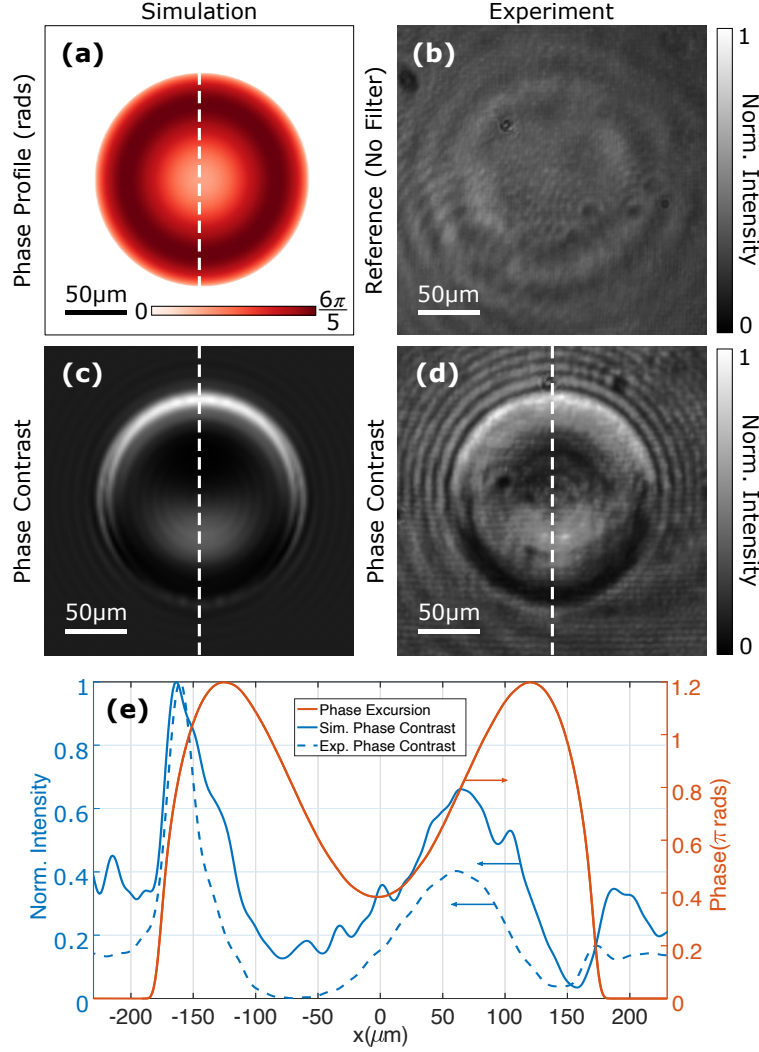


FIG. 4. A red blood cell (a) was emulated by a spatial light modulator with a phase excursion of $6\pi/5$. Simulated and experimental images normalized to their brightest pixels are given in (b)-(d), comprising control (b), simulated (c) and experimental (d) phase contrast images. These are supported by line profiles in (e) along the dashed lines shown in (b)-(d).

without needing to access the Fourier plane. The transfer function exhibited the required behaviour for high-pass filtering enabling edge detection, in addition to approximately linear regions allowing phase visualization through spatial differentiation. Rotating the filter enabled access to these regimes to offset the Fourier origin in k -space. Phase gradients were converted into intensity variations to generate images with significantly enhanced contrast. As a result, notch filters offer a new approach to non-interferometric phase visualization through image processing without bulky or expensive components.

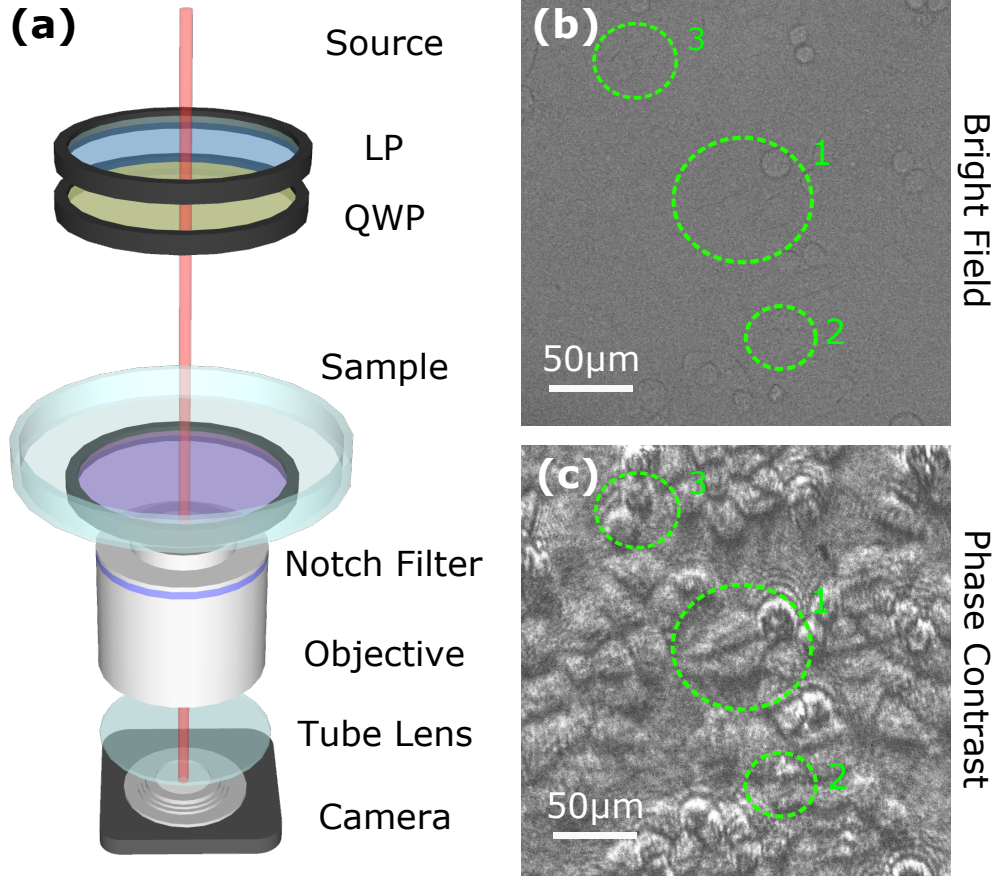


FIG. 5. An experimental schematic for biological phase imaging is given in (a) and outlined in the supplementary information (§S2D). A bright field image of the HeLa cells obtained without the filter is given in (b). The corresponding phase contrast image obtained using the filter is given in (c).

Commercial notch filters offer a relatively cost efficient and readily available option for phase visualization compared to alternative optics. Although the band-stop region was limited within the visible band, various filters have been designed with coverage across the electromagnetic spectrum. For example, Yuan et al.⁴² presented a photonic filter employable at the absorption band of acetylene gas. Others include terahertz⁴³, infrared⁴⁴, microwave^{45,46} and commercial ultra-violet filters. These hold potential for phase imaging across the spectrum using the methods outlined in this paper, with applications in machine vision and biological imaging beyond the visible range. Live biological monitoring is possible with the notch filter dynamically capturing phase information of specimens. Further applications include integration into conventional CMOS sensors to form spatial frequency and phase-sensitive detectors. Incorporating notch filters into their detection planes would introduce spatial frequency selectivity and phase variations in otherwise

indiscriminate, intensity-based devices.

Although phase contrast was produced by the notch filter, its behaviour in the contrast zone was not perfectly linear. Furthermore, its restricted numerical aperture limits the range of samples to which it could be applied. The large angular range of the suppression zone also restricts contrast to sufficiently sharp features. Not only is the range of objects limited, but it necessitates rotation of the notch filter. Finally, our theoretical and numerical modelling neglected the non-negligible notch filter thickness, which can introduce perturbations into the beam path. This can lead to the appearance of aberrations such as those in the edge enhanced images in the supplementary information (§S2B). However, the success of experiments performed here provide confidence that custom thin film devices could be developed with reduced thicknesses to minimize aberrations and tailor the transfer function.

IV. CONCLUSION

In conclusion, this paper has demonstrated real-time, all-optical, object-plane image processing using a commercial spectral notch filter. Spectroscopic measurements verified angle dispersive band-rejection necessary for high-pass spatial frequency filtering and phase contrast imaging. Edge detection was realizable through the suppression zone where unscattered field components were removed. Meanwhile, offsetting to approximately linear regions within the contrast zone produced phase contrast images. Unstained biological samples, including human cervical cancer cells, imposing otherwise invisible phase modulations were visualized by the filter. Given its real-time capabilities, this has significant implications in label-free biomedical imaging⁴⁷ including medical diagnostics, non-invasive micro-organism growth and dynamical monitoring. The results open developmental possibilities in extending to beyond the visible band and constructing monolithic spatial frequency-sensitive cameras for commercialization.

FUNDING

This research was funded by the Australian Government through the Australian Research Council Centre of Excellence grant (CE200100010). S.B.S also gratefully acknowledges the support of the Ernst & Grace Matthaei Scholarship and the Australian Government Research Training Program Scholarship.

SUPPLEMENTARY MATERIAL

Supporting information is available in the supplementary material, including the underlying theory and detailed experimental methods.

REFERENCES

- ¹F. Zernike, “Phase contrast, a new method for the microscopic observation of transparent objects,” *Physica* **9**, 686–698 (1942).
- ²W. Lang, *Nomarski Differential Interference-Contrast Microscopy* (Carl Zeiss, 1982).
- ³E. Balaur, G. A. Cadenazzi, N. Anthony, A. Spurling, E. Hanssen, J. Orian, K. A. Nugent, B. S. Parker, and B. Abbey, “Plasmon-induced enhancement of ptychographic phase microscopy via sub-surface nanoaperture arrays,” *Nature Photonics* **15**, 222–229 (2021).
- ⁴R. Horstmeyer, J. Chung, X. Ou, G. Zheng, and C. Yang, “Diffraction tomography with fourier ptychography,” *Optica* **3**, 827–835 (2016).
- ⁵K. Giewekemeyer, P. Thibault, S. Kalbfleisch, A. Beerlink, C. M. Kewish, M. Dierolf, F. Pfeiffer, and T. Salditt, “Quantitative biological imaging by ptychographic x-ray diffraction microscopy,” *Proceedings of the National Academy of Sciences* **107**, 529–534 (2010).
- ⁶E. Engay, D. Huo, R. Malureanu, A.-I. Bunea, and A. Lavrinenko, “Polarization-dependent all-dielectric metasurface for single-shot quantitative phase imaging,” *Nano Letters* **21**, 3820–3826 (2021).
- ⁷E. Bostan, E. Froustey, M. Nilchian, D. Sage, and M. Unser, “Variational phase imaging using the transport-of-intensity equation,” *IEEE Transactions on Image Processing* **25**, 807–817 (2016).
- ⁸J. Li, Q. Chen, J. Sun, J. Zhang, and C. Zuo, “Multimodal computational microscopy based on transport of intensity equation,” *Journal of Biomedical Optics* **21**, 126003 (2016).
- ⁹R. W. Gerchberg and W. O. Saxton, “A practical algorithm for the determination of phase from image and diffraction plane pictures,” *Optik* **35**, 237–246 (1972).
- ¹⁰J. R. Fienup, “Reconstruction of an object from the modulus of its fourier transform,” *Optics Letters* **3**, 27–29 (1978).
- ¹¹L. Wesemann, E. Panchenko, K. Singh, E. D. Gaspera, D. E. Gómez, T. J. Davis, and A. Roberts, “Selective near-perfect absorbing mirror as a spatial frequency filter for optical image processing,” *APL Photonics* **4**, 100801 (2019).

- ¹²T. Zhu, Y. Zhou, Y. Lou, H. Ye, M. Qiu, Z. Ruan, and S. Fan, “Plasmonic computing of spatial differentiation,” *Nature Communications* **8**, 15391 (2017).
- ¹³L. Wesemann, T. J. Davis, and A. Roberts, “Meta-optical and thin film devices for all-optical information processing,” *Applied Physics Reviews* **8**, 031309 (2021).
- ¹⁴J. W. Goodman, *Introduction to Fourier Optics* (McGraw-Hill, 1996).
- ¹⁵T. J. Davis, F. Eftekhari, D. E. Gómez, and A. Roberts, “Metasurfaces with asymmetric optical transfer functions for optical signal processing,” *Physical Review Letters* **123**, 013901 (2019).
- ¹⁶A. Roberts, D. E. Gomez, and T. J. Davis, “Optical image processing with metasurface dark modes,” *Journal of the Optical Society of America A* **35**, 1575–1584 (2018).
- ¹⁷G. Hui, H. Ruyong, W. Chaopeng, L. Zequn, W. Le, and Z. Shengmei, “Compressed ghost edge imaging,” *Chinese Optics Letters* **17**, 071101 (2019).
- ¹⁸T. Brosnan and D.-W. Sun, “Improving quality inspection of food products by computer vision—a review,” *Journal of Food Engineering* **61**, 3–16 (2004), applications of computer vision in the food industry.
- ¹⁹K. Park, M. Chae, and J. H. Cho, “Image pre-processing method of machine learning for edge detection with image signal processor enhancement,” *Micromachines* **12** (2021), 10.3390/mi12010073.
- ²⁰J. W. Goodman, *Statistical Optics* (John Wiley & Sons, 2000).
- ²¹A. Silva, F. Monticone, G. Castaldi, V. Galdi, A. Alù, and N. Engheta, “Performing mathematical operations with metamaterials,” *Science* **343**, 160–163 (2014).
- ²²Y. Zhou, H. Zheng, I. I. Kravchenko, and J. Valentine, “Flat optics for image differentiation,” *Nature Photonics* **14**, 316–323 (2020).
- ²³L. Wesemann, J. Rickett, J. Song, J. Lou, E. Hinde, T. J. Davis, and A. Roberts, “Nanophotonics enhanced coverslip for phase imaging in biology,” *Light: Science & Applications* **10**, 98 (2021).
- ²⁴L. Wan, D. Pan, S. Yang, W. Zhang, A. A. Potapov, X. Wu, W. Liu, T. Feng, and Z. Li, “Optical analog computing of spatial differentiation and edge detection with dielectric metasurfaces,” *Optics Letters* **45**, 2070–2073 (2020).
- ²⁵A. Komar, R. A. Aoni, L. Xu, M. Rahmani, A. E. Miroshnichenko, and D. N. Neshev, “Edge detection with mie-resonant dielectric metasurfaces,” *ACS Photonics* **8**, 864–871 (2021).
- ²⁶A. Cordaro, H. Kwon, D. Sounas, A. F. Koenderink, A. Alù, and A. Polman, “High-index dielectric metasurfaces performing mathematical operations,” *Nano Letters* **19**, 8418–8423 (2019).

- ²⁷T. Zhu, Y. Lou, Y. Zhou, J. Zhang, J. Huang, Y. Li, H. Luo, S. Wen, S. Zhu, Q. Gong, M. Qiu, and Z. Ruan, “Generalized spatial differentiation from the spin hall effect of light and its application in image processing of edge detection,” *Phys. Rev. Applied* **11**, 034043 (2019).
- ²⁸L. Wesemann, J. Rickett, T. J. Davis, and A. Roberts, “Real-time phase imaging with an asymmetric transfer function metasurface,” *ACS Photonics* **9**, 1803–1807 (2022).
- ²⁹D. Pan, L. Wan, M. Ouyang, W. Zhang, A. A. Potapov, W. Liu, Z. Liang, T. Feng, and Z. Li, “Laplace metasurfaces for optical analog computing based on quasi-bound states in the continuum,” *Photonics Research* **9**, 1758–1766 (2021).
- ³⁰S. K. Case, “Fourier processing in the object plane,” *Opt. Lett.* **4**, 286–288 (1979).
- ³¹G. Indebetouw, “Tunable spatial filtering with a fabry-perot etalon,” *Applied Optics* **19**, 761–764 (1980).
- ³²G. Molesini and F. Quercioli, “Interference filters as fourier processors,” *Applied Optics* **20**, 1893–1893 (1981).
- ³³G. Molesini, D. Bertani, and M. Cetica, “Dark ground microscopy with detuned interference filters,” *Optical Engineering* **21**, 1061 – 1063 (1982).
- ³⁴M. Cetica, D. Bertani, and G. Molesini, “Interference filters for fourier filtering and for frequency coding,” *Journal of Non-Crystalline Solids* **47**, 279–281 (1982).
- ³⁵G. Indebetouw and T.-C. Poon, “Incoherent spatial filtering with a scanning heterodyne system,” *Appl. Opt.* **23**, 4571–4574 (1984).
- ³⁶D. K. Angell, “Incoherent spatial filtering with grating interferometers,” *Appl. Opt.* **24**, 2903–2906 (1985).
- ³⁷D. Peri and D. Ritter, “Spatial filtering with volume gratings,” *Appl. Opt.* **24**, 1535–1540 (1985).
- ³⁸A. Márquez, C. Neipp, A. Beléndez, S. Gallego, M. O. no, and I. Pascual, “Edge-enhanced imaging with polyvinyl alcohol /acrylamide photopolymer gratings,” *Opt. Lett.* **28**, 1510–1512 (2003).
- ³⁹C. A. F. Marques, V. de Oliveira, H. J. Kalinowski, and R. N. Nogueira, “Production of optical notch filters with fine parameter control using regenerated fiber bragg gratings,” *Opt. Lett.* **37**, 1697–1699 (2012).
- ⁴⁰G. Antonacci, K. Elsayad, and D. Polli, “On-chip notch filter on a silicon nitride ring resonator for brillouin spectroscopy,” *ACS Photonics* **9**, 772–777 (2022).
- ⁴¹E. Evans and Y.-C. Fung, “Improved measurements of the erythrocyte geometry,” *Microvascular Research* **4**, 335–347 (1972).

- ⁴²Z. Yuan, X. Lou, and Y. Dong, “Microwave photonic notch filter with a tunable frequency and a bandwidth based on gas absorption,” *Optics Letters* **45**, 248–251 (2020).
- ⁴³H. S. Bark, K.-H. Jang, K. Lee, Y. U. Jeong, and T.-I. Jeon, “Thz guided-mode resonance notch filter with variable filtering strength,” *Scientific Reports* **11**, 1307 (2021).
- ⁴⁴M.-S. Kwon and S.-Y. Shin, “Tunable notch filter using a thermooptic long-period grating,” *J. Lightwave Technol.* **22**, 1968 (2004).
- ⁴⁵Y. Long, J. Xia, Y. Zhang, J. Dong, and J. Wang, “Photonic crystal nanocavity assisted rejection ratio tunable notch microwave photonic filter,” *Scientific Reports* **7**, 40223 (2017).
- ⁴⁶S. Gertler, N. T. Otterstrom, M. Gehl, A. L. Starbuck, C. M. Dallo, A. T. Pomerene, D. C. Trotter, A. L. Lentine, and P. T. Rakich, “Narrowband microwave-photonic notch filters using brillouin-based signal transduction in silicon,” *Nature Communications* **13**, 1947 (2022).
- ⁴⁷Y. Park, C. Depeursinge, and G. Popescu, “Quantitative phase imaging in biomedicine,” *Nature Photonics* **12**, 578–589 (2018).

Supplementary Material

S1. THEORETICAL MODELLING

A. Phase Visualization via Spatial Frequency Filtering

The core idea underlying this work is to directly modify spatial frequencies of wavefields without accessing Fourier planes to enable phase extraction. The essential feature of suitable devices is a sensitivity to angles of incidence. As explained in the main article, this associates with a selective transmission to spatial frequencies necessary for image processing.

Image processing for phase visualization can be explained using classical scalar electromagnetic theory¹. Polarization effects can be accounted through tensorial analysis², but are ignored here for simplicity. Suppose that the source electric field can be modelled as monochromatic plane waves $E_s(x, y, z)$ of wavelength λ and wavevector $\vec{k} = (k_x, k_y, k_z)$. With the z -axis as the optical axis, k_x and k_y denote the transverse spatial frequency components and $k_0 \equiv |\vec{k}| = \frac{2\pi}{\lambda}$ is the wavenumber. The source illuminates a weakly absorbing object located in the $z = 0$ plane, which is assumed as optically thin in the Kirchhoff approximation. Its transmitted light can be modelled by

$$E_{\text{obj}}(x, y, 0) = O(x, y)E_s(x, y, 0) , \quad (4)$$

where the object transmission function is approximately given by

$$O(x, y) \approx O_0 e^{i\varphi(x, y)} . \quad (5)$$

Its intensity image $|O(x, y)|^2 = |O_0|^2$ has little to no contrast by construction and is therefore referred to as a phase object. Therefore, its visualization requires access to the phase function $\varphi(x, y)$ that contains its shape information. This is made possible through optical systems, such as thin films^{3,4}, described by specific optical transfer functions that can extract $\varphi(x, y)$ from the complex exponential of Eq. (5). To shed light on this, we note the following property for the

Fourier transform of derivatives,

$$\mathcal{F} \left\{ \frac{\partial^m E}{\partial x^m} + \frac{\partial^m E}{\partial y^m} \right\} (k_x, k_y) = i^m (k_x^m + k_y^m) \mathcal{F} \{ E(x, y) \} (k_x, k_y) , \quad (6)$$

where \mathcal{F} denotes the Fourier transform and $m \in \mathbb{N}$. As in Eq. (1) of the main article, the object light filtered by the notch filter is related to its optical transfer function $\mathcal{H}(k_x, k_y)$,

$$E_{\text{out}}(x, y, 0) = \mathcal{F}^{-1} \{ \mathcal{H}(k_x, k_y) \mathcal{F} \{ E_{\text{obj}}(x', y', 0) \} (k_x, k_y) \} (x, y) , \quad (7)$$

where the notch filter is taken to immediately succeed the object. By comparing Eqs. (6) and (7), the m^{th} -order derivatives of the input field are produced if the optical transfer function is given by

$$\mathcal{H}(k_x, k_y) = \begin{cases} i^m k_x^m, & \text{for x-differentiation} \\ i^m k_y^m, & \text{for y-differentiation} \end{cases}, \quad (8)$$

up to a multiplicative constant. It was shown in the main article that the transfer function exhibited approximately linear variation within the contrast zone. The notch filter is therefore capable of approximate first-order spatial differentiation in this region required for phase contrast imaging. Substituting a linear optical transfer function into Eq. (7) and taking $E_s(x, y, 0) = \text{const.}$ produces Eq. (3) of the main article, given by

$$\nabla O(x, y) \approx iO_0 (\nabla \phi(x, y)) e^{i\phi(x, y)}. \quad (9)$$

Phase gradients of the object are translated into measurable intensity variations described by the amplitude term in Eq. (9). Thus, its intensity image is now given by

$$|\nabla O(x, y)|^2 \approx |\nabla \phi(x, y)|^2, \quad (10)$$

with contrast generated where $\nabla \phi \neq 0$. This holds for approximately pure phase objects, with the gradient taken along the axis of rotation. However, non-negligible amplitude variations in $O(x, y)$ would produce additional amplitude derivatives in Eq. (9). Although, it is possible to subtract these by using measured intensities in the absence of the filter to isolate the phase contribution.

B. Simulations

Numerical simulations were performed in Python by implementing the theoretical model presented in §S2.1. Our experimentally measured modulation transfer function and the phase response provided the manufacturer were combined to model the optical response of the notch filter.

S2. EXPERIMENTAL METHODS

A. Transfer Function Determination

Spectroscopic measurements of the notch filter (Thorlabs NF633-25) were made using the experimental configuration depicted in Fig. 1 of the main article. The filter was 3.5 mm thick and

comprised tantalum pentoxide (Ta_2O_5) and silicon dioxide (SiO_2) thin films on a fused quartz substrate. White light from a fibre-coupled (Thorlabs SM600 single-mode fibre) halogen lamp (Ocean Insight HL-2000-FHSA) was collimated by a microscope objective (Nikon UPlanFL 20x/0.15NA). This light was polarized by a linear polarizer (Thorlabs LPVIS050-MP) to produce p or s -polarized light. Circularly polarized light was produced by introducing an additional quarter waveplate (Thorlabs AQWP05M-600) before illuminating the notch filter. A plano-convex lens (Thorlabs LA1068-A, $f = 75$ mm) focused the transmitted light onto a port that was fibre-coupled (Thorlabs M15L01) to a spectrometer (Ocean Insight QE6500). Measurements of transmission spectra were made for incident angles ranging from -30° to 30° by incrementally rotating the filter by 2° .

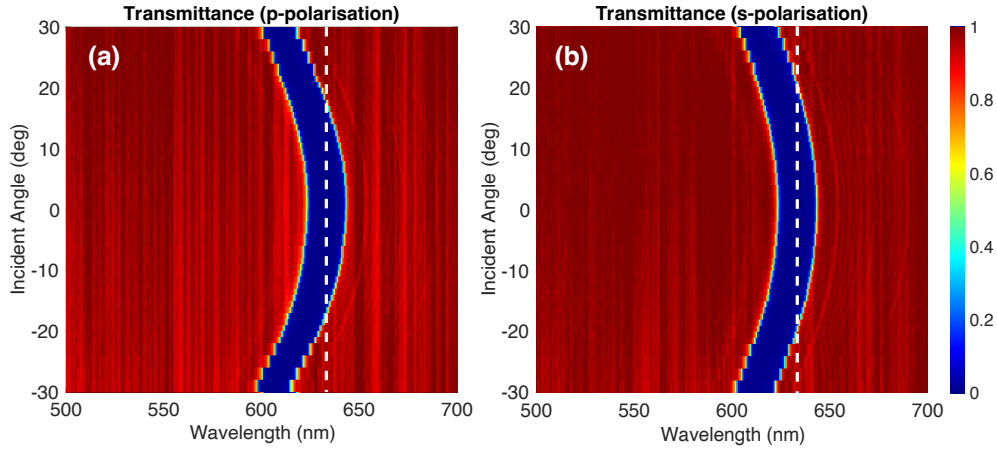


FIG. 6. Transmission spectra of the notch filter obtained with p - and s -polarized light are given in (a) and (b), respectively. These exhibit similar behaviour with suppression around 633 nm (dashed lines) that blue-shifts with increasing incident angle.

Spectra were collected for p -, s - and circularly polarized light. The former two are given in Fig. 6, while the latter is given in Fig. 2(a) of the main article. Each of these confirm suppression about the band-stop wavelength and its angular dispersion.

B. Edge Detection

All-optical amplitude image processing was experimentally performed to demonstrate edge detection with the notch filter. As depicted in Fig. 7, fibre-coupled (Thorlabs SM600) laser light (Thorlabs S1FC635 635 nm) was collimated by a microscope objective (Nikon LU Plan

5x/0.15NA) and two lenses (Thorlabs LB1901-B $f = 75$ mm & Thorlabs LB1761-B $f = 25.4$ mm). Light reflected from a mirror was projected onto the the largest regions of a USAF resolution test target (Thorlabs R2L2S1N1 NBS 1963A) using a second microscope objective (Olympus UPlanFI 20x/0.50NA) and lens (Thorlabs LA1509-A $f = 100$ mm). Upon reflection from a second mirror, a fourth lens (Thorlabs LA1433-A $f = 150$ mm) allowed image filtering with the notch filter between paired microscope objectives (Nikon UPlanFI 20x/0.4NA & Nikon LU Plan 50x/0.55NA). Finally, a fifth lens (Thorlabs LA1131-A $f = 50$ mm) projected the filtered light onto a camera (Thorlabs DCC1645C).

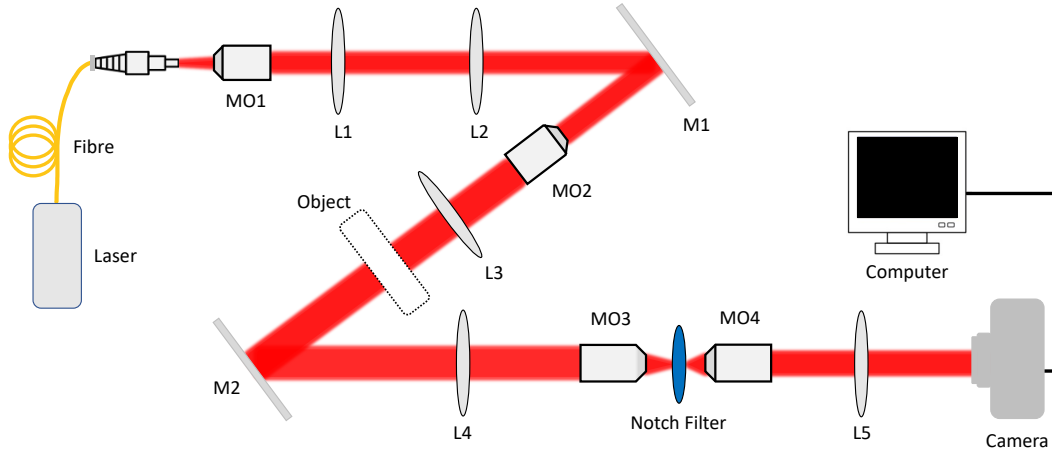


FIG. 7. A schematic of the experimental configuration for edge detection with a notch filter is shown. Here L, MO and M each denote lenses, microscope objectives and mirrors, respectively.

Given in Figs. 8(a) and (b), the simulated and experimental results demonstrate edge enhancement produced by the notch filter. The uniform intensity regions associated with unscattered field components were removed while retaining only the edges. This is supported by line profiles given in Fig. 8(c). Some slight asymmetries are present in the experimental edge-enhanced image owing to small rotations of the filter.

C. Phase Imaging

All-optical image processing for phase visualization was performed using the configuration given in Fig. 3 of the main article. Fibre-coupled (Thorlabs SM600) laser light (Thorlabs S1FC635, 635 nm) was collimated by a microscope objective (Nikon LU Plan 5x/0.15NA) and two plano-convex lenses (Thorlabs LA1027-A $f = 75$ mm and Thorlabs LA1509-A $f = 100$ mm).

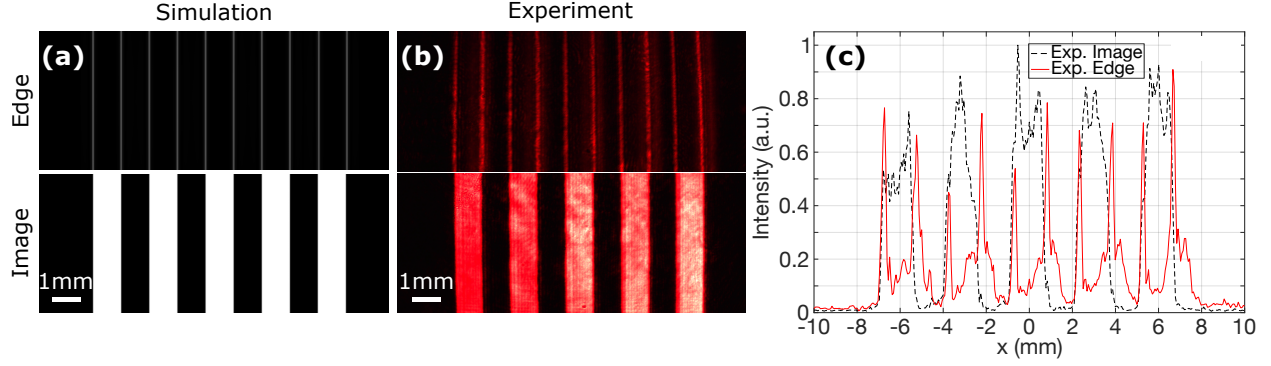


FIG. 8. Edge-enhanced images of USAF test target bars overlayed on their unfiltered images are given in (a) and (b). Line profiles in (c) depict suppression within the uniform regions of the bars.

Required for its operation, a linear polarizer (Thorlabs LPVIS050-MP) ensured that linearly polarized light illuminated a reflective spatial light modulator (Holoeye Pluto-2-VIS-014 LCOS-SLM). Comprising 1920×1080 liquid crystal pixels of $8 \mu\text{m}$ pitch, it prescribed computer-generated phase profiles of human red blood cells. The reflected light from the SLM passed through a quarter wave-plate (Thorlabs AQWP05M-600) to circularly polarize it. A third plano-convex lens (Thorlabs LA1433-A $f = 150 \text{ mm}$) and microscope objective (Olympus PlanN 20x/0.4NA) together formed a telescope that de-magnified the SLM image onto the notch filter in its focal plane. To access the contrast zone, the latter was longitudinally rotated by 14° using a rotation mount. A second, identical microscope objective (Olympus PlanN 20x/0.4NA) and a fourth plano-convex lens (Thorlabs LA1131-A $f = 50 \text{ mm}$) re-magnified and focused the filtered image onto a camera (Thorlabs DCC1645C).

D. Phase Microscopy

Bright field and phase contrast microscopy of the HeLa cells were performed using the configuration given in Fig. 5(a) of the main article. First, bright field images were obtained using white light from an inverted microscope (Nikon Ti-80i) without the notch filter. The source was then replaced by fibre-coupled (Thorlabs SM600) laser light (Thorlabs S1FC635 635 nm) collimated by an objective (Olympus A4 4x/0.1NA), and circularly polarized by a linear polarizer (Thorlabs LPVISC100-MP2) and quarter waveplate (Thorlabs AQWP05M-600). These were contained within an optical cage mounted on an XYZ-stage to vary incident angles. Moreover, the notch filter was placed immediately beneath the sample to perform phase imaging. A second

microscope objective (Nikon LU Plan 50x/LWD) collected the filtered light onto a camera (Andor Zyla sCMOS 4.2P). Given in Fig. 9(b), a differential interference contrast microscopy image was taken on a second microscope (Olympus BX60) using a separate microscope objective (Olympus PlanN 20x/0.4NA).

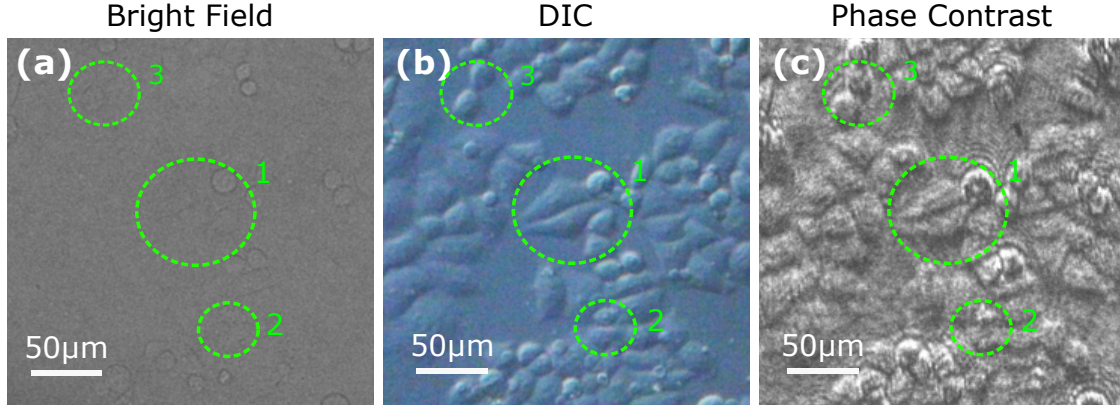


FIG. 9. A differential interference contrast microscopy image of the HeLa cells is given in (b). For comparison purposes, its bright field image (a) and experimental phase contrast image obtained with the notch filter (c) are reproduced from the main article.

E. Biological Sample Preparation

The HeLa cells were grown in Dulbecco's modified Eagle's medium (DMEM) (Lonza) supplemented with 10% heat inactivated bovine growth serum (Gibco), 1x Pen-Strep (Lonza) at 37 °C with 5% carbon dioxide. The cells were plated 24 h before fixation onto 35 mm glass bottom dishes, before being fixed with 4% paraformaldehyde for 15 min at room temperature and washed 3 times with phosphate-buffered saline (PBS).

REFERENCES

- ¹A. Roberts, D. E. Gomez, and T. J. Davis, "Optical image processing with metasurface dark modes," *Journal of the Optical Society of America A* **35**, 1575–1584 (2018).
- ²L. Wesemann, T. J. Davis, and A. Roberts, "Meta-optical and thin film devices for all-optical information processing," *Applied Physics Reviews* **8**, 031309 (2021).

- ³T. Zhu, Y. Zhou, Y. Lou, H. Ye, M. Qiu, Z. Ruan, and S. Fan, “Plasmonic computing of spatial differentiation,” *Nature Communications* **8**, 15391 (2017).
- ⁴L. Wesemann, E. Panchenko, K. Singh, E. D. Gaspera, D. E. Gómez, T. J. Davis, and A. Roberts, “Selective near-perfect absorbing mirror as a spatial frequency filter for optical image processing,” *APL Photonics* **4**, 100801 (2019).